1.0

4.5
5.0
5.6
6.3

1.1

1.25

2.8
3.2
3.6
4.0

1.4

2.5
2.2
2.0
1.8

1.6

MICROCOPY RESOLUTION TEST CHART
NATIONAL BUREAU OF STANDARDS-1963-A

# AIAA'84

**AD–A159 596**

**AIAA-84-0254**
**Numerical Simulation of the Interaction of a Vortex with Stationary Airfoil in Transonic Flow**

G.R. Srinivasan, Flow Simulations Inc., Sunnyvale, CA; and W.J. McCroskey and P. Kutler, NASA Ames Research Center, Moffett Field, CA

DTIC
ELECTE
SEP 2 4 1985
S D

# AIAA 22nd Aerospace Sciences Meeting
## January 9-12, 1984/Reno, Nevada

**85** 9

# AIAA'84

## AD-A159 596

### AIAA-84-0254
**Numerical Simulation of the Interaction of a Vortex with Stationary Airfoil in Transonic Flow**

G.R. Srinivasan, Flow Simulations Inc., Sunnyvale, CA; and W.J. McCroskey and P. Kutler, NASA Ames Research Center, Moffett Field, CA

DTIC
ELECTE
SEP 2 4 1985
S D

## AIAA 22nd Aerospace Sciences Meeting
### January 9-12, 1984/Reno, Nevada

85  9  23  11

Fig. 13  Instantaneous pressure distributions during an airfoil-vortex unsteady interaction:  NACA 64A006 airfoil, $M_\infty = 0.85$, $\alpha = 0°$, $\Gamma = 0.2$, $y_v = -0.26$.



Fig. 14  Lift and pitching-moment variations with instantaneous  x-position of the vortex for the conditions of Fig. 13.
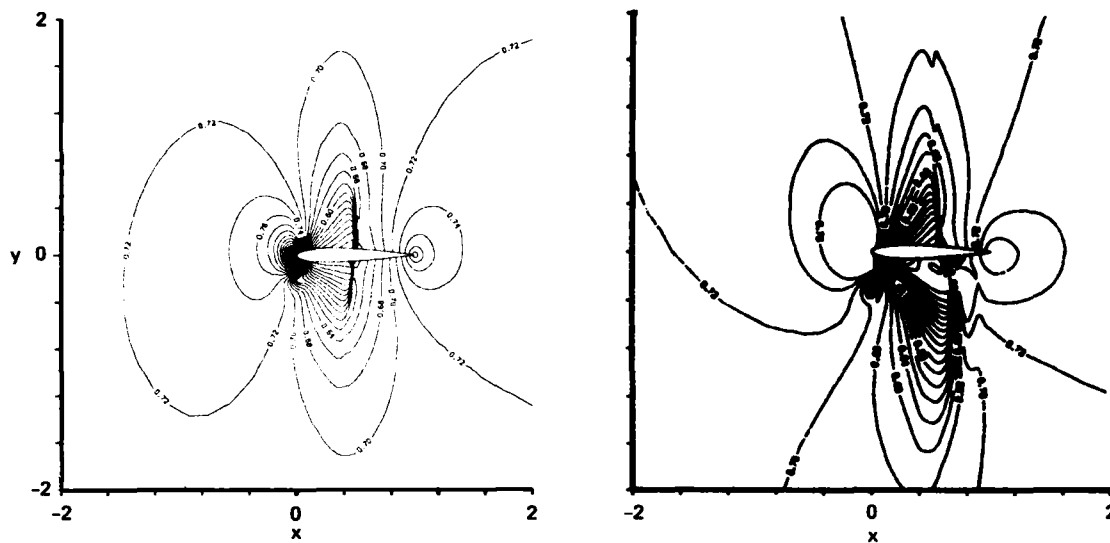
(c) Pressure contours.

Fig. 11 Concluded.
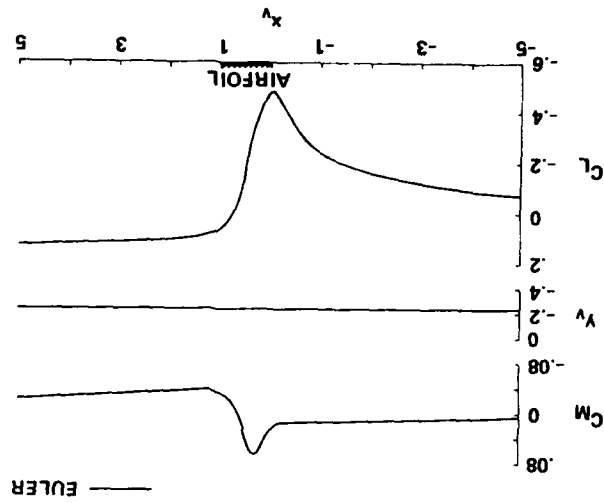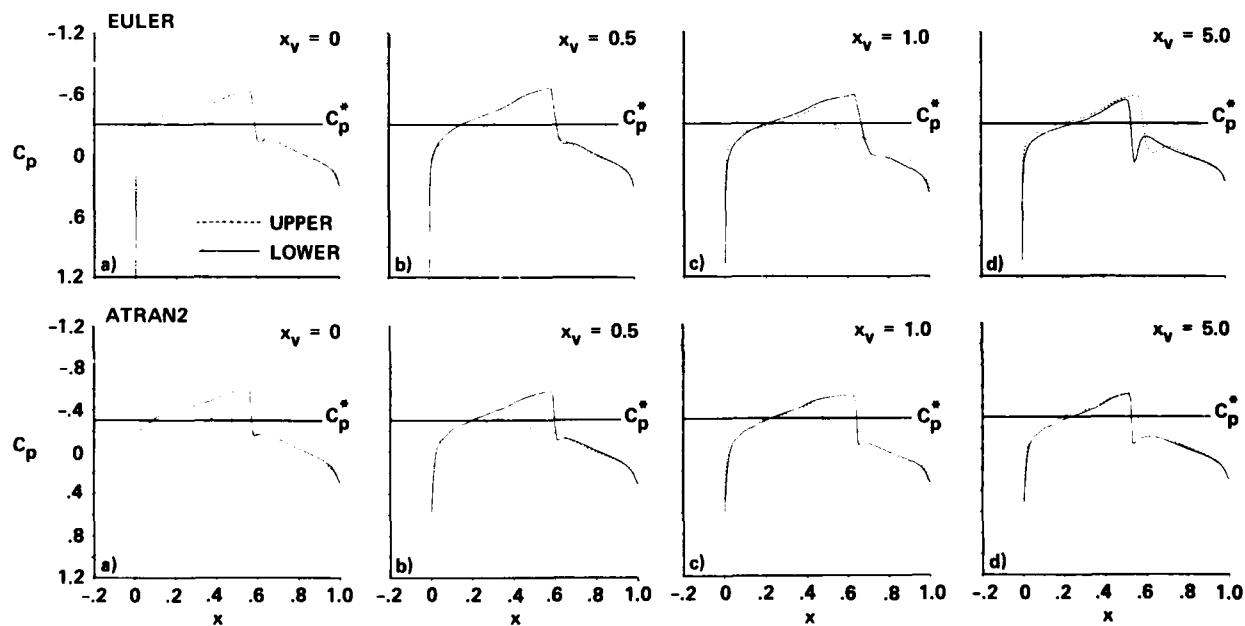


Fig. 12 Instantaneous pressure distributions during an airfoil-vortex unsteady interaction: NACA 64A006 airfoil, $M_\infty = 0.85$, $\alpha = 0°$, $\Gamma = 0.2$, $y_v = -0.52$.

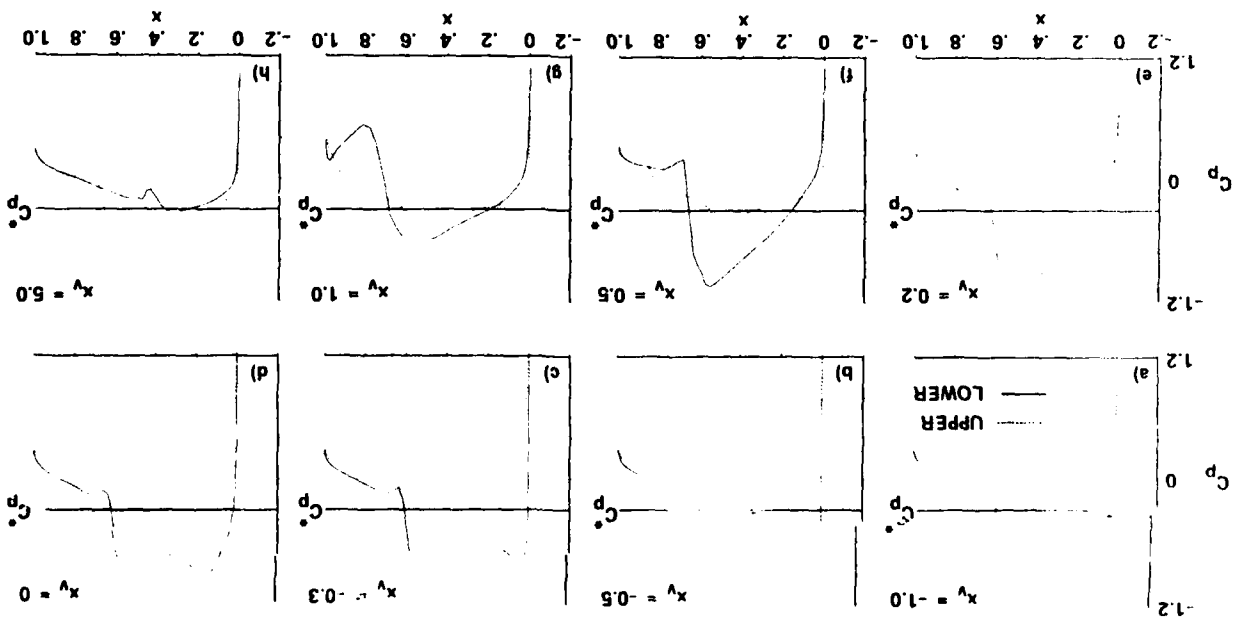UNSTEADY (VORTEX FREE)　　　QUASI-STEADY (VORTEX FIXED)
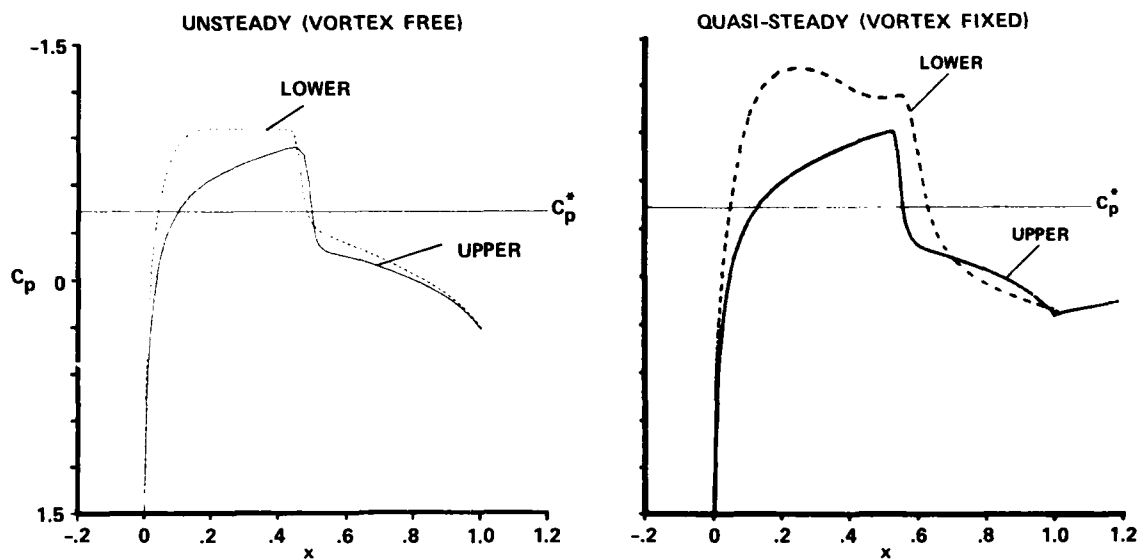


(a) Pressure distribution.
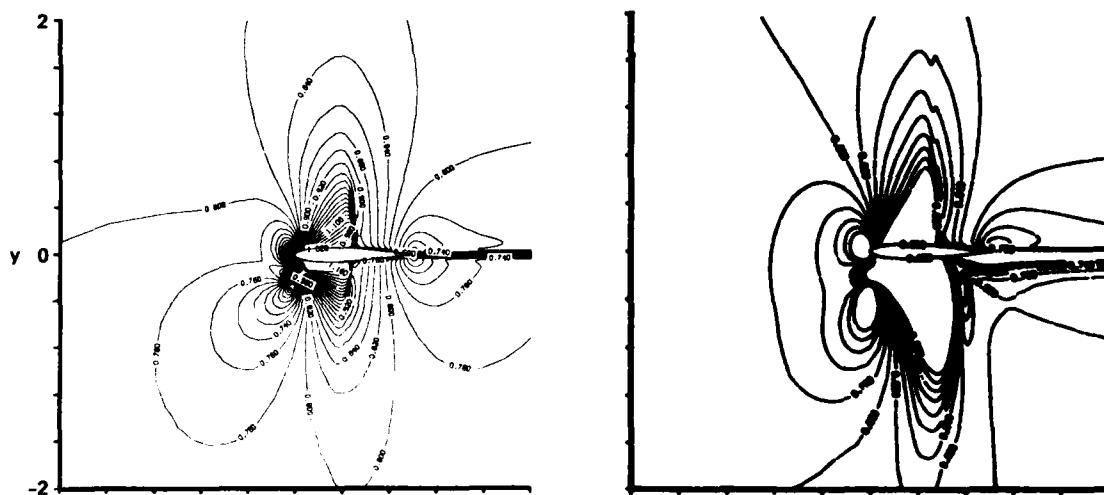


(b) Mach number contours.

Fig. 11 Comparison of the unsteady and quasi-steady thin-layer Navier-Stokes solutions of the vortex-airfoil interaction: NACA 0012 airfoil, $M_\infty = 0.8$, $\alpha = 0.5°$, Re = 5.78 mil/ft, $\Gamma = 0.2$, for unsteady case $x_v = 0$, $y_v = 0.26$, for quasi-steady case $x_o = 0$, $y_o = -0.26$.
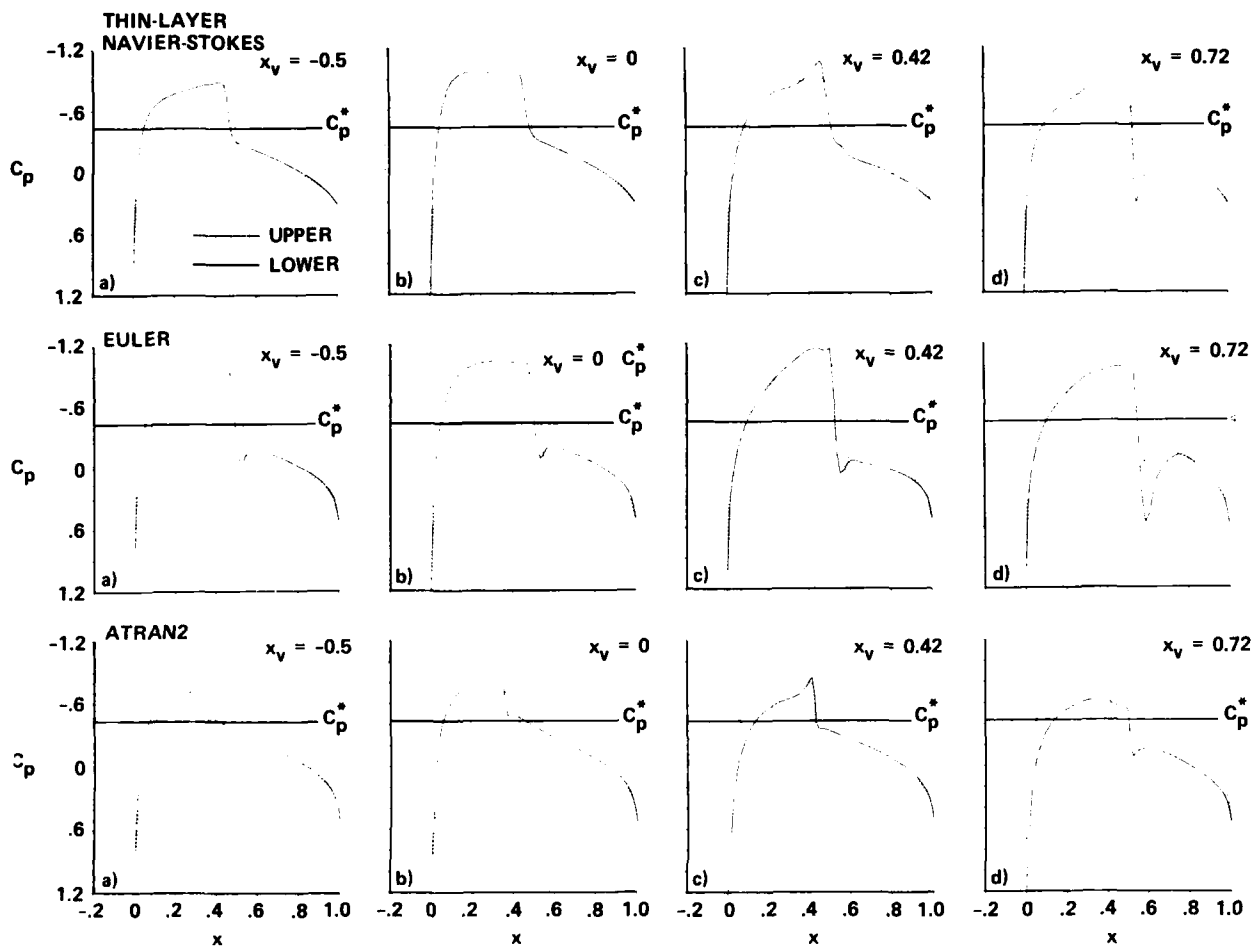
Fig. 9   Instantaneous pressure distributions during an airfoil-vortex unsteady interaction:   NACA 0012 airfoil, $M_\infty = 0.8$, $\alpha = 0.5°$, Re = 4.78 mil/ft, $\Gamma = 0.2$ ($C_{LV} = 0.4$), $x_o = -5.5$, $y_o = -0.26$, and $y_v = y_o - (x_v - x_o) \tan \alpha$.
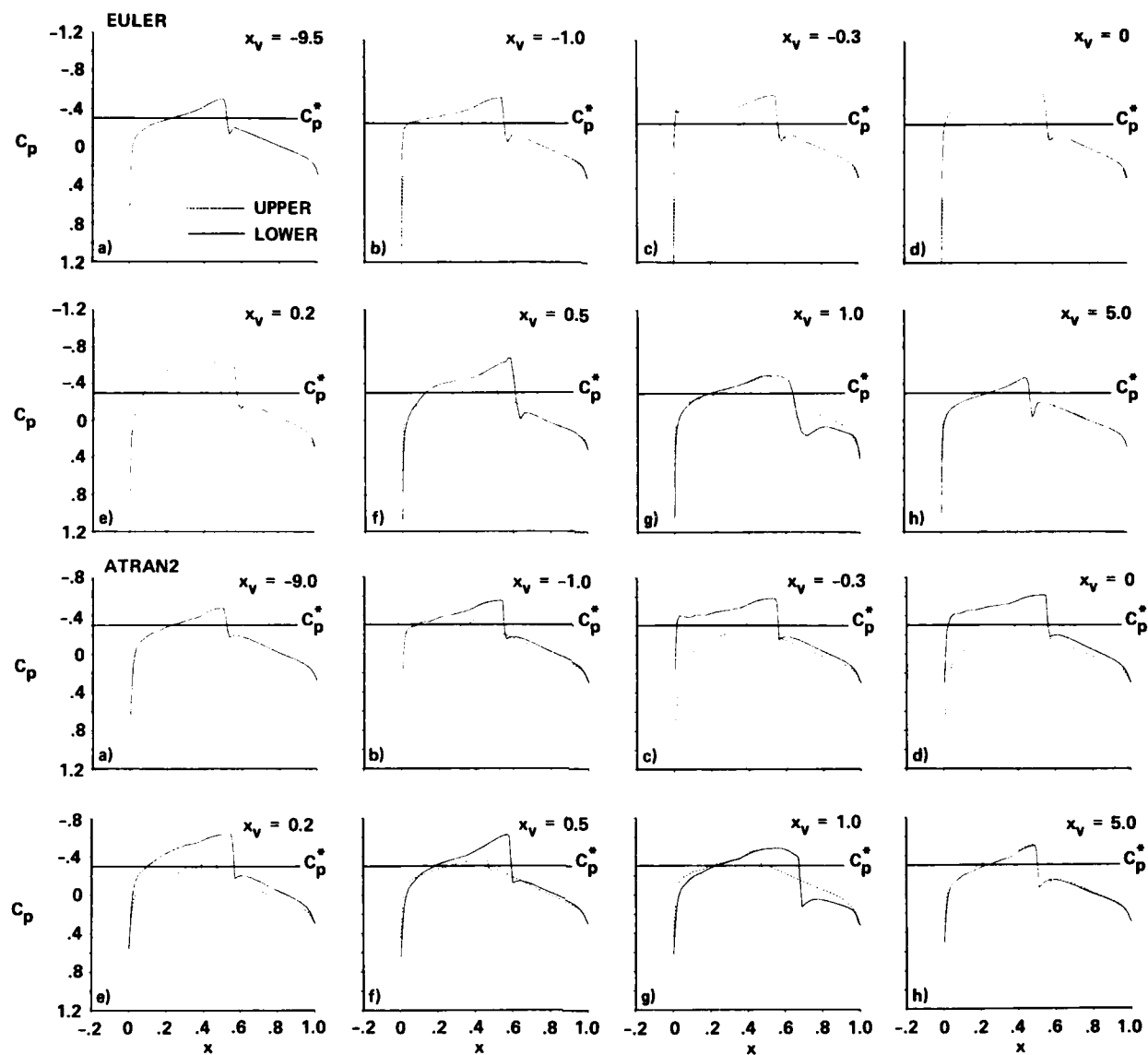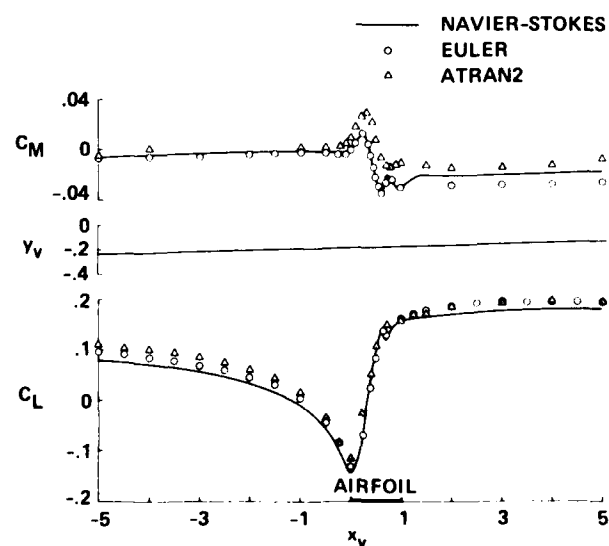
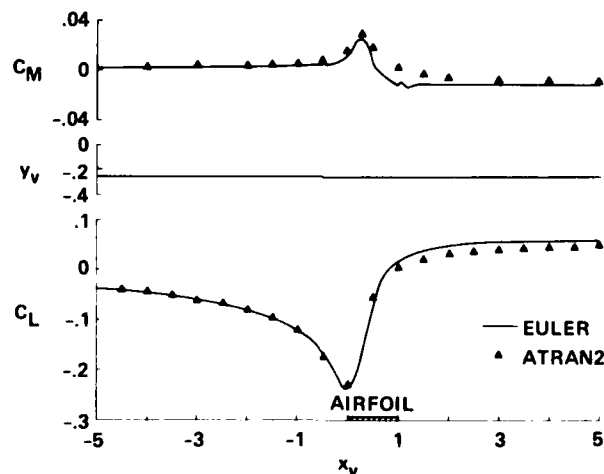

Fig. 10   Lift and pitching-moment variations with instantaneous   x-position of the vortex for the conditions of Fig. 9.

15

(a) Vortex fixed (quasi-steady).　　　　　　(b) Vortex convecting at $Q_\infty$ (unsteady).
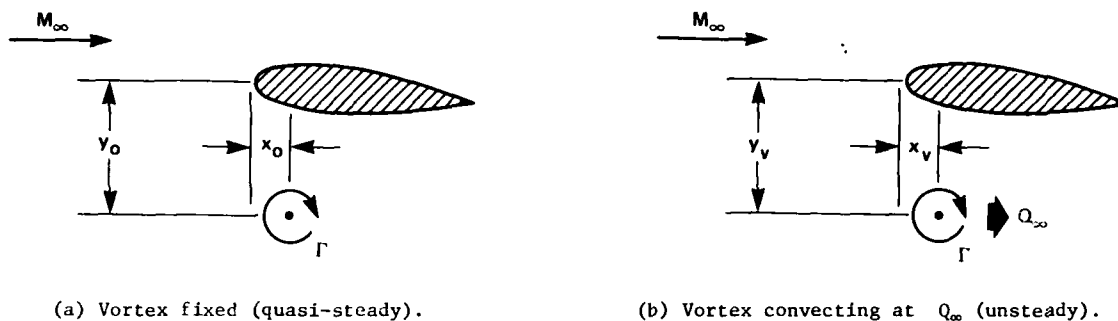
Fig. 7　Schematic of the vortex interaction configurations considered.



(a) Thin-layer Navier-Stokes.　　　　(b) Euler.　　　　　(c) ATRAN2.
$C_L = 0.0576$, $C_D = 0.0146$.　　$C_L = 0.0604$, $C_D = 0.0118$.　　$C_L = 0.1000$, $C_D = 0.0192$.
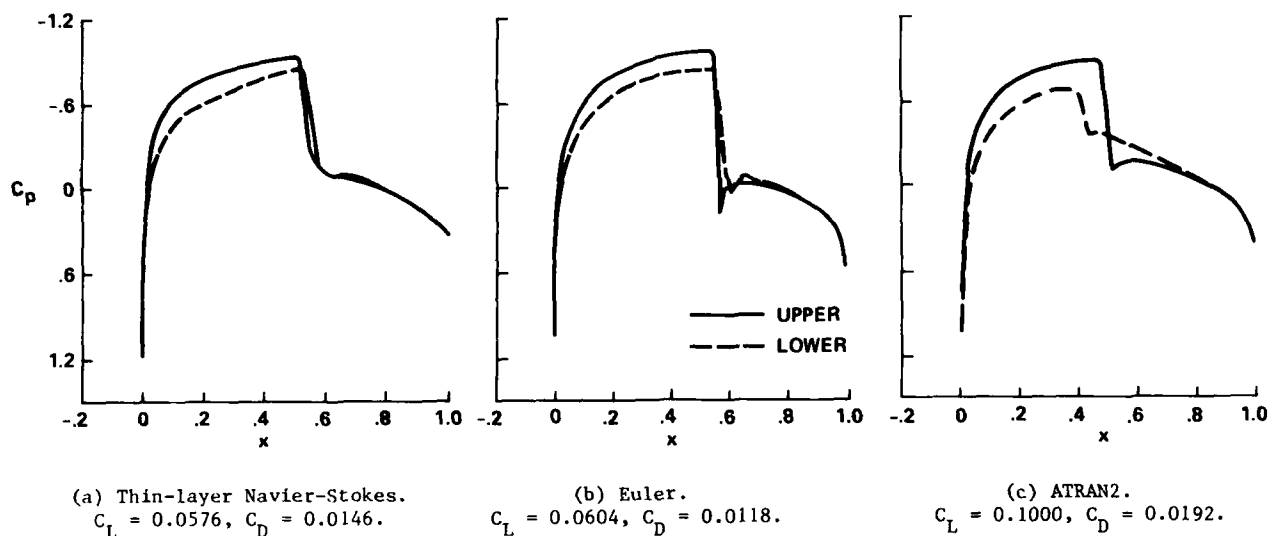
Fig. 8　Quasi-steady pressure distributions of the interaction of a fixed vortex with NACA 0012 airfoil: $M_\infty = 0.8$, $\alpha = 0.5°$, Re = 5.78 mil/ft, $\Gamma = 0.065$ ($C_{LV} = 0.13$), $x_o = 0.5$, $y_o = -1$.

14

(a) Without modification.

(b) With modification.
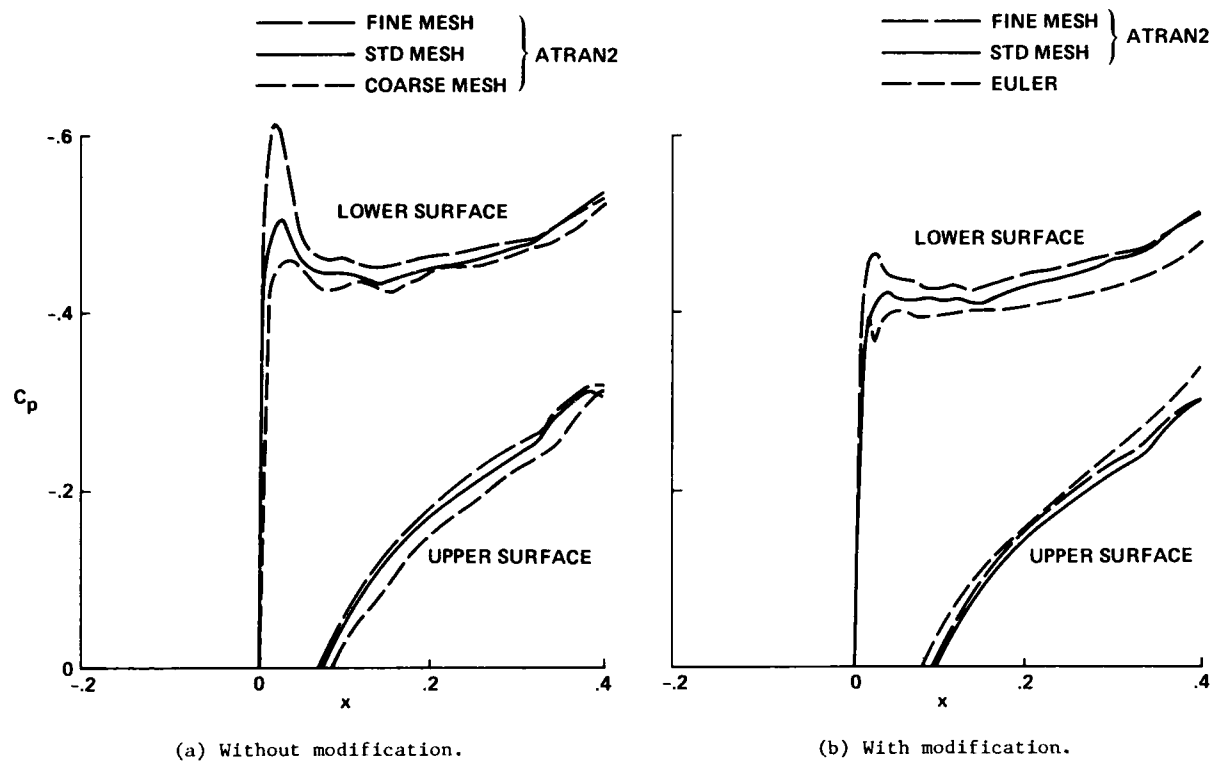
Fig. 5 Pressure distributions in the leading edge region for the NACA 64A006 airfoil with and without leading edge modification in ATRAN2 code: $M_\infty = 0.85$, $\alpha = 0°$, $\Gamma = 0.2$ ($C_{LV} = 0.4$), $x_v = -0.3$, $y_v = 0.26$. Between $x = -0.05$ to $0$ and $x = 0$ to $0.05$ and at $y = 0$, the grids have the following number of grid points: coarse mesh has $5 + 9$; standard mesh has $8 + 9$; fine mesh has $8 + 25$; while the Euler grid has 31 points between $x = 0$ and $0.05$.
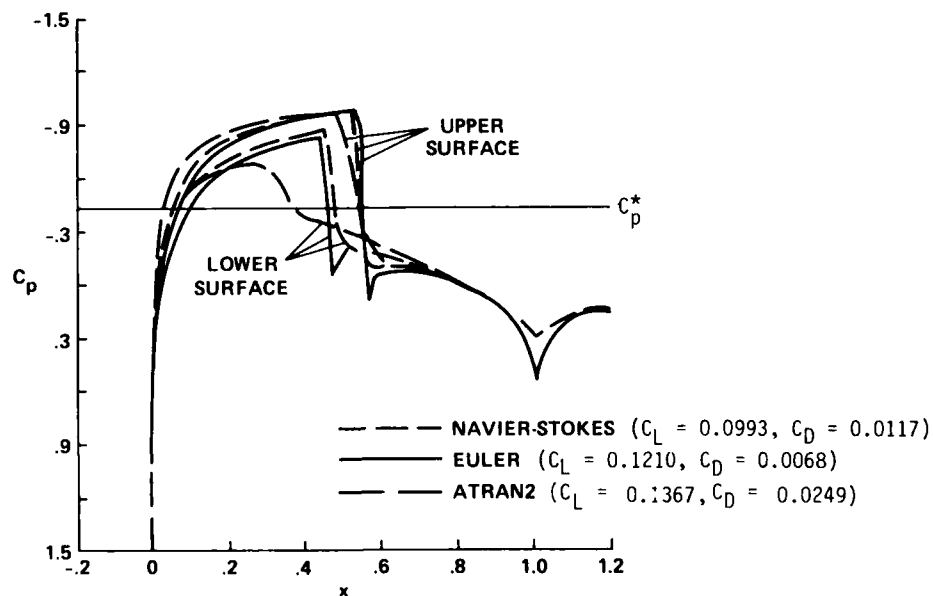


Fig. 6 Baseline pressure distribution for NACA 0012 airfoil: $M_\infty = 0.8$, $\alpha = 0.5°$, Re - 5.78 mil/ft.

13
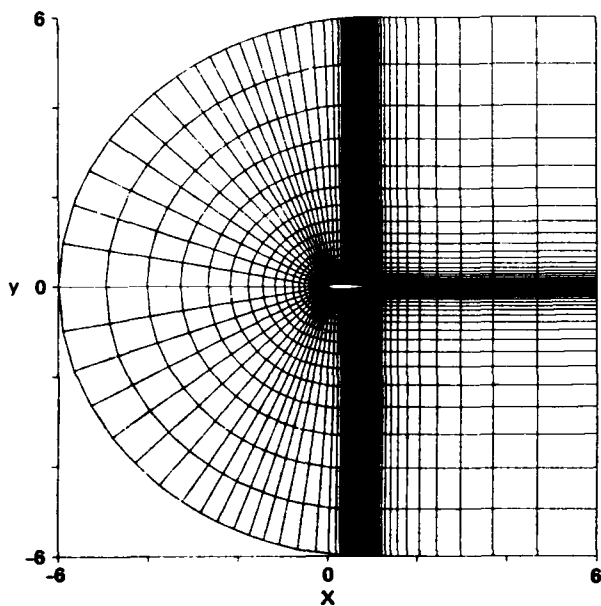
(a) Farfield view of viscous 161 × 52 C-grid for NACA 0012 airfoil.
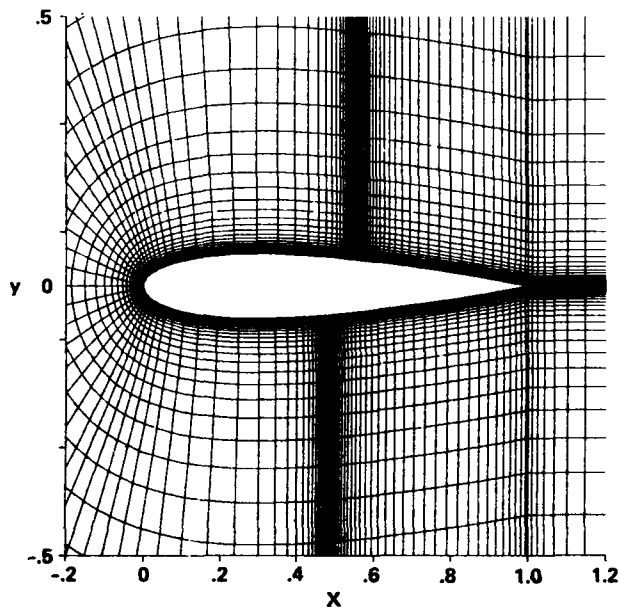
(b) Nearfield view of viscous 161 × 52 C-grid for NACA 0012 airfoil.
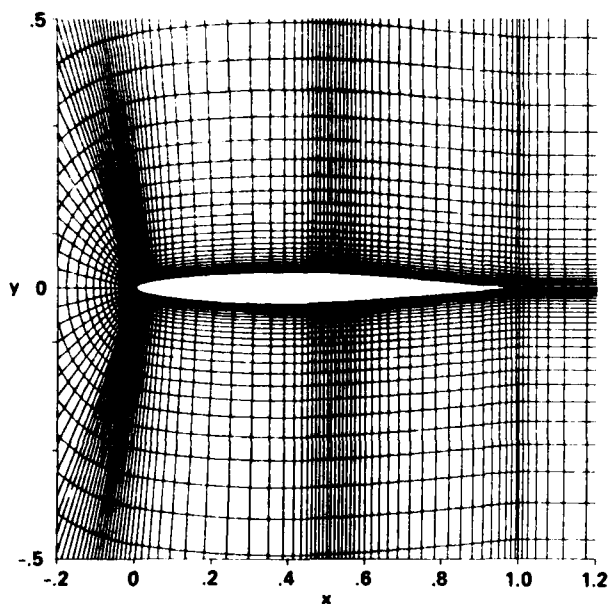
(c) Nearfield view of Euler 181 × 45 C-grid for NACA 64A006 airfoil.
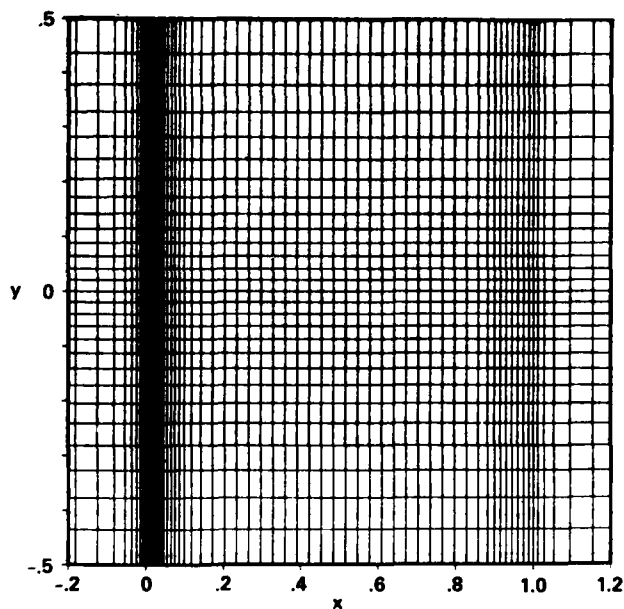
(d) Nearfield view of ATRAN2 126 × 97 square grid for NACA 64A006 airfoil.

Fig. 4  Typical computational grids for viscous and inviscid flow field calculations.

12
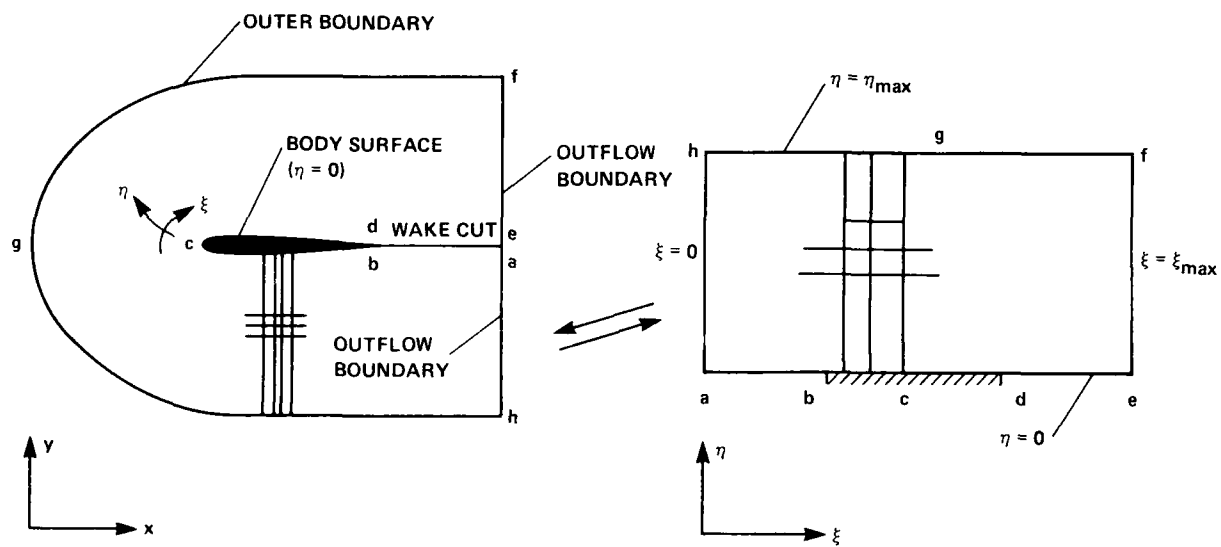
Fig. 3  Physical and computational planes.

[23]Kefitz, B. L., Melnik, R. E., and Grossman, B., "An Analysis of the Leading-Edge Singularity in Transonic Small-Disturbance Theory," Quarterly Journal of Mechanics and Applied Mathematics, Vol. XXXI, Part 3, May 1978, pp. 137-155.

[24]van Dyke, M. D., "Second-Order Subsonic Airfoil Theory Including Edge Effects," NACA Report 1274, 1956.

[25]Shapiro, A. H., The Dynamics and Thermodynamics of Compressible Fluid Flow, Vol. I, 1953, Roland Press, New York, pp. 315-326.

[26]Srinivasan, G. R., "Interaction of a Vortex with Stationary Rotorcraft Airfoil in Transonic Flow," Flow Simulations, Inc. Report No. 83-02, April 1983.

[27]Parathasarathy, R., "Aerodynamic Sound Generation Due to Vortex-Airfoil Interaction," Ph.D. Dissertation, Stanford Univ., Spet. 1972.

(a) VORTEX PARALLEL TO LEADING EDGE



(b) VORTEX PARALLEL TO FREE STREAM
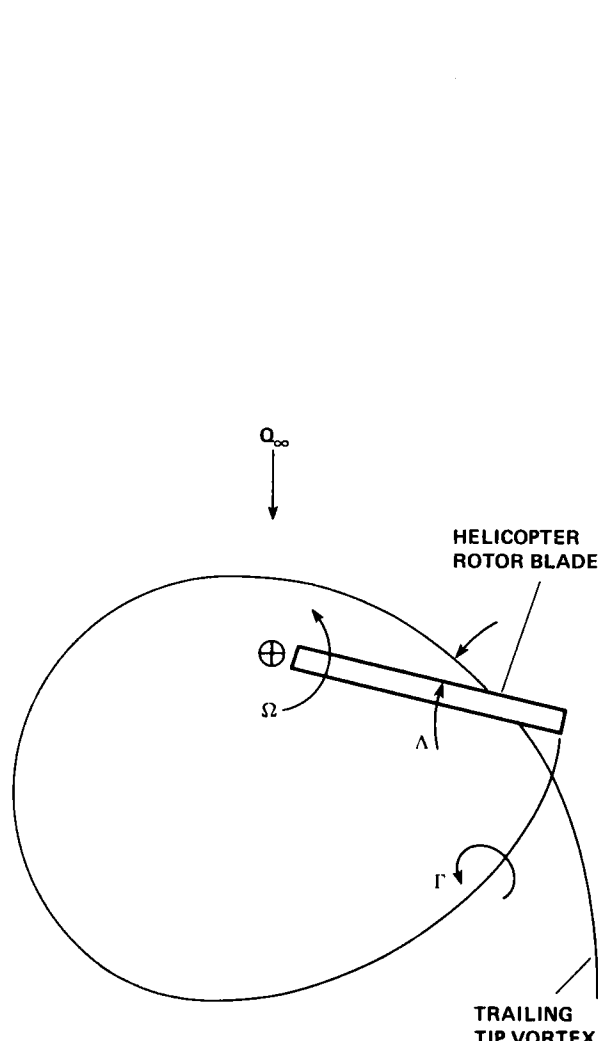
Fig. 1 Schematic of helicopter-rotor-blade/vortex interaction.
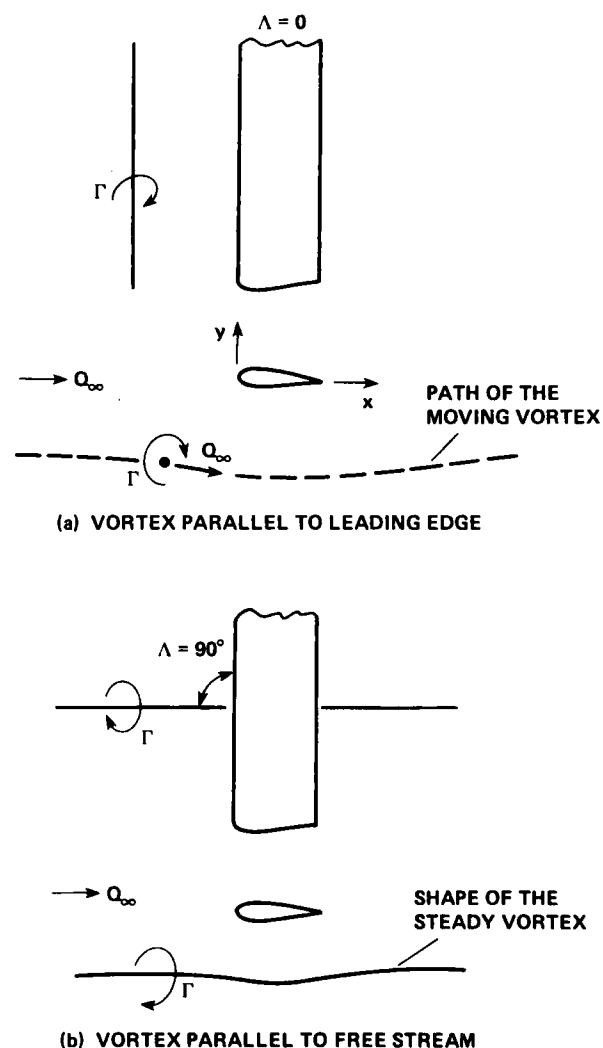
Fig. 2 Limiting cases of blade-vortex interaction problem.

For the stronger interactions considered in this paper, strong in the sense of exceeding the small disturbance limit, the Euler solutions showed a sharp suction peak in the pressure distributions in the leading edge region followed by a rapid compression-like wave when the interacting vortex was approximately within one chord upstream of the leading edge of the NACA 64A006 airfoil.

In all cases, the results show a tremendous influence of the vortex on the flow field around the airfoil. This is particularly true when the vortex is stationary. For a convecting vortex, the most dramatic changes in the airfoil flow field seem to occur when the vortex is within one chord ahead of the leading edge of the airfoil.

The small disturbance code runs approximately 20 times faster than the Euler and thin-layer Navier-Stokes codes. However, the latter were found to be more accurate and robust with important consequences for the stronger interaction cases considered here.

## References

[1]George, A. R. and Chang, S. B., "Noise Due to Transonic Blade-Vortex Interactions," American Helicopter Society Paper A-83-39-50-D000, May 1983.

[2]Steger, J. L., "Implicit Finite-Difference Simulation of Flow about Arbitrary Two-Dimensional Geometries," AIAA Journal, Vol. 16, No. 7, July 1978, pp. 679-686.

[3]Buning, P. G. and Steger, J. L., "Solution of the Two-Dimensional Euler Equations with Generalized Coordinate Transformation Using Flux Vector Splitting," AIAA Paper 82-0971, AIAA/ASME 3rd Joint Thermophysics, Fluids, Plasma and Heat Transfer Conference, June 1982, St. Louis, Missouri.

[4]McCroskey, W. J. and Goorjian, P. M., "Interactions of Airfoils with Gusts and Concentrated Vortices in Unsteady Transonic Flow," AIAA Paper 83-1691, AIAA 16th Fluid and Plasma Dynamics Conference, July 1983, Danvers, Massachusetts.

[5]Ballhaus, W. F. and Goorjian, P. M., "Implicit Finite-Difference Computations of Unsteady Transonic Flows about Airfoils," AIAA Journal, Vol. 15, No. 12, Dec. 1977, pp. 1728-1735.

[6]"Equations, Tables, and Charts for Compressible Flow," NACA Report 1135 Ames Research Staff, 1941.

[7]Baldwin, B. S. and Lomax, H., "Thin Layer Approximation and Algebraic Model for Separated Turbulent Flows," AIAA Paper 78-257, AIAA 16th Aerospace Sciences Meeting, Jan. 1978, Huntsville, Alabama.

[8]Lamb, H., Hydrodynamics, 6th ed., Dover, New York, p. 592.

[9]Srinivasan, G. R. and Steger, J. L., "Computation of Wing-Vortex Interaction in Transonic Flow Using Implicit Finite Difference Algorithm," NASA CR-166251, March 1981.

[10]Sorenson, R. L., "A Computer Program to Generate Two-Dimensional Grids About Airfoils and Other Shapes by the Use of Poisson's Equation," NASA TM-81198, May 1980.

[11]Steger, J. L. and Chaussee, D. S., "Generation of Body-Fitted Coordinates Using Hyperbolic Partial Differential Equations," SIAM J. Sci. Stat. Comput., Vol. 1, No. 4, Dec. 1980, pp. 431-437.

[12]Pulliam, T. H., Jespersen, D. C., and Childs, R. E., "An Enhanced Version of an Implicit Code for the Euler Equations," AIAA Paper 83-0344, AIAA 21st Aerospace Sciences Meeting, Jan. 1983, Reno, Nevada.

[13]Eiseman, P. R., "Geometric Methods in Computational Fluid Dynamics," ICASE Report No. 80-11, April 1980.

[14]Lindemuth, I., and Killeen, I., "Alternating Direction Implicit Techniques for Two-Dimensional Magnetohydrodynamics Calculations," J. of Comp. Physics, Vol. 13, 1973, pp. 181-208.

[15]Briley, W. F. and McDonald, H., "An Implicit Numerical Method for the Multi-Dimensional Compressible Navier-Stokes Equations," Report No. 911363-6, United Aircraft Research Laboratories, 1973.

[16]Briley, W. R. and McDonald, H., "Solution of the Three-Dimensional Compressible Navier-Stokes Equations by an Implicit Technique," Lecture Notes in Physics, No. 35, Proceedings of the Fourth International Conference on Numerical Methods in Fluid Dynamics, ed., R. D. Richtmyer, Boulder, Colorado, June 1974, pp. 105-110.

[17]Beam, R. M. and Warming, R. F., "An Implicit Finite-Difference Algorithm for Hyperbolic Systems in Conservation-Law Form," J. of Comp. Physics, Vol. 22, Sept. 1976, pp. 87-109.

[18]Beam, R. and Warming, R. F., "An Implicit Factored Scheme for the Compressible Navier-Stokes Equations," AIAA Paper 77-645, June 1977, Albuquerque, New Mexico.

[19]Steger, J. L. and Kutler, P., "Implicit Finite-Difference Procedures for the Computation of Vortex Wakes," AIAA Journal, Vol. 15, No. 4, April 1977, pp. 581-590.

[20]Kutler, P., Chaussee, D., and Pulliam, T., "Supersonic Flow Over Ablated Nosetips Using an Implicit Unsteady Euler Equation Solver," Paper presented at the Open Forum Session of the AIAA 10th Fluid and Plasma Dynamics Conference, June 1977, Albuquerque, New Mexico.

[21]Srinivasan, G. R., Chyu, W. J., and Steger, J. L., "Computation of Simple Three-Dimensional Wing Vortex Interaction in Transonic Flow," AIAA Paper 81-1206, AIAA 14th Fluid and Plasma Dynamics Conference, June 1981, Palo Alto, California.

[22]Pulliam, T. H. and Steger, J. L., "On Implicit Finite-Difference Simulations of Three-Dimensional Flow," AIAA Journal, Vol. 18, No. 2, Feb. 1980, pp. 159-167.

Figure 12 shows $C_p$ plots for the Case 1 where the vortex of strength $\Gamma = 0.2$ is initially located at $x_0 = -9.5$ and $y_0 = -0.52$. Euler and ATRAN2 codes predict pressure fields which are in qualitative agreement. As before, the influence of the vortex on the airfoil flow field begins for vortex position upstream and continues until the vortex is downstream of the airfoil. However, the most rapid and dramatic changes occur when the vortex is between one chord length upstream of the leading edge of the airfoil and the trailing edge. From the $C_p$ plots presented in Fig. 12 for the vortex location at the leading edge and downstream of this, it can be seen that both Euler and ATRAN2 solutions show large similarities at all x-stations; even the shock waves on upper and lower surfaces are quite sharp for the two solutions.

Figures 13 and 14 show a similar comparison of $C_p$ plots for Case 2 where the vortex of strength $\Gamma = 0.2$ was initially located at the same x-location of $x_0 = -9.5$ but closer to the airfoil at $y_0 = -0.26$. For this particular set of conditions, the interaction is quite severe in terms of the small disturbance approximation. The ATRAN2 numerical solution seems to be marginally stable depending on the fineness of the grid geometry and on the size of the time step $\Delta t$.

The pressure distributions on the airfoil are shown for this case at eight x-stations of vortex position for the two methods of calculations in Fig. 13. As before, the dramatic changes occur when the vortex is within one chord from the airfoil leading edge. Before the modification of the surface boundary condition in the leading edge region, Eq. (17), was made for the ATRAN2 code, the code predicted a rapid development of a sharp suction peak followed by a rapid compression-like wave in the leading edge region. However, with the modified boundary condition, Eq. (19), the magnitude of the peak was dramatically reduced as pointed out in Section 2.6. With this the Euler and ATRAN2 codes predict results which are in good qualitative agreement. Even the gross aerodynamic quantities are in very good agreement as seen in Fig. 14 where lift and moment coefficients are shown as a function of the vortex position for this interaction.

Figure 15 shows a similar type of pressure distribution plots as Fig. 13 but for Case 3 where the vortex is located initially at the same location as Case 2 but doubled in strength. The rest of the conditions are identical to that of Case 2. No ATRAN2 results were obtained for this case as these conditions are quite severe and exceed the limits of small-disturbance approximation.

Pressure distributions are presented for the interaction history at eight x-stations of vortex location. As before, the trend of events is similar to that shown in Figs. 12 and 13. The sharp suction peak of the pressure distribution at the leading edge, mentioned before, is the most noteworthy event occurring for the vortex location within one chord from the airfoil leading edge (e.g., x = -0.5). Using the transonic small disturbance code without leading edge correction for the surface boundary condition, both George and Chang[1] and McCroskey and Goorjian[4] in independent investigations have observed this kind of leading edge behavior even for the weaker vortex case mentioned above (Figs. 12 and 13), and they concluded that this is possibly responsible for a "blade-slap"-like acoustic wave

propagation. In contract, as shown by the results presented here, the Euler code predicts this kind of leading edge effect only for stronger interactions.

Figure 16 shows the lift and moment coefficient plots as a function of vortex location for this interaction.

The description of the flow field during the unsteady interaction process is delineated in Fig. 17 in the form of Mach number and pressure contour plots. The effect of doubling the vortex strength is shown in Figs. 17a-17d. Figures 17a and 17b show contour plots for Case 2 ($\Gamma = 0.2$) when the vortex location is one chord upstream of the leading edge of the airfoil. Figures 17c and 17d are for Case 3 ($\Gamma = 0.4$) and at the same vortex location. The shock wave location and its movement due to doubling the vortex strength are apparent from these plots. Figures 17c and 17d are for Case 3 ($\Gamma = 0.4$) but for the case when the vortex is at $x_v = 0.2$ (right below the airfoil). Comparison of these figures with Figs. 17c and 17d shows a tremendous movement of the lower surface shock wave and modification of the leading edge flow as the vortex passes by. The Mach contour upper limit is fixed at 1.2 in these plots and this enables one to visualize the progressive decrease of lower surface pressure on the airfoil as is evident from the corresponding increase of the local Mach number of the flow field.

## 4. Summary and Conclusions

A two-dimensional numerical simulation of the interaction of a concentrated vortex with a stationary rotorcraft airfoil in transonic flow has been studied. Three different computational methods, which solve the thin-layer Navier-Stokes, Euler, and Transonic Small Disturbance equations, were used. The NACA 0012 and NACA 64A006 profiles were selected for the airfoil shape. The interacting vortex, having a Lamb-like velocity distribution, was introduced as a perturbation of the mean flow into the governing equations. The equations were then solved implicitly for the interacting flow field. The required computational grids were generated by an algebraic grid generation scheme. Typical run times for these computational methods on the NASA Ames Research Center CRAY X-MP machine, expressed as CPU time per time step per grid node, were as follows: thin-layer Navier-Stokes $= 2.1 \times 10^{-4}$ sec, Euler $= 1.8 \times 10^{-4}$ sec, and Transonic Small Disturbance $= 1.0 \times 10^{-5}$ sec.

Most of the interactions considered in this paper are strong, in the sense that the vortex produced significant and nonlinear distortions of the flow field, but relatively weak in the sense that they are within the scope of the transonic small disturbance assumptions. For such cases, whether the vortex was stationary or moving, the three computational methods gave qualitatively similar results. The close agreement of the thin-layer Navier-Stokes and Euler results indicates that viscous effects are negligible for these interactions. In general, ATRAN2 results are in good agreement with the results from the other two methods, although needing a special leading edge treatment for thin airfoils; without this treatment, ATRAN2 results overpredicted the interaction effects in the leading edge region. In this sense, previous studies[1,4] of such interactions using the transonic small disturbance method are in error.

8

Fig. 6, shows the dramatic influence of the vortex on the airfoil flow field. Since the vortex induces spacially varying downwash downstream and upwash upstream of its location and also positive streamwise velocity above and negative stream velocity below its location (because of the sense of its rotation, see Fig. 7), its influence on the airfoil flow field is determined by where it is located with respect to airfoil. The shock wave on the lower surface has moved downstream with all three methods of computation, ATRAN2 showing much larger influence than the other two methods. Evidently the small disturbance, irrotational approximation to Euler equations introduces errors in the solution.

Figure 8 also lists the coefficient of lift and drag values. Comparison of these numbers shows the extent of the vortex influence on the flow field of the airfoil. For example, the lift and drag coefficients for the baseline viscous case are respectively 0.09928 and 0.01173; with the vortex interaction these values change to $C_L = 0.05757$ and $C_D = 0.01457$.

(b) Vortex Convecting with the Flow. So far, the results of vortex interaction with an airfoil were presented where the vortex was fixed at one location in the flow field. In this section, the vortex is made to convect freely at free stream velocity $Q_\infty$ as shown in Fig. 7b and allowed to interact with the flow field around the airfoil. This case approximately simulates a practical flow situation on a helicopter blade in contrast to the fixed vortex case.

For a moving vortex in compressible flow, the cylindrical velocity distribution is given by Eq. (10). The velocity from Eq. (10) and the pressure field from Eq. (11) induced by the vortex are introduced through the vector $\hat{q}_0$ in Eq. (15) as done for fixed vortex case before.

To compute the interaction flow field, the vortex is initially positioned at, say, the upstream grid boundary or any suitable upstream location $(x_0, y_0)$ of the airfoil and then made to convect with the flow at the free stream velocity and along a straight line aligned with the free stream. Typical resulting solution of such an interaction for the case of vortex of strength $\Gamma = 0.2(C_{LV} = 0.4)$ initially located at $x_0 = -5.5$ and $y_0 = -0.26$ and moving with the free stream velocity is presented in the form of $C_p$ plots in Fig. 9 at several stages of vortex passage across the airfoil. The pressure distribution ($C_p$) presented in Fig. 9 generally typifies the history of interaction of the airfoil flow field as the vortex passes by. The three methods of computations used here give results which are in qualitative agreement. More results for interactions involving vortex of different strengths are detailed in the report of Srinivasan.[26]

Examination of the pressure distributions of Fig. 9 show the expected initial development of the pressure difference from the baseline case to resemble the case of increasing negative angle of attack (downwash influence) as the vortex is approaching the airfoil. This influence changes to that of a positive angle of attack (upwash) as the vortex passes behind the airfoil. Although the initial influence of the approaching vortex is felt by the airfoil when the vortex is only a few chords upstream of it, its influence decays very slowly even when the vortex has passed many chords down-

stream of it, and the return of the flow around the airfoil to the original state is an extremely slow process. This is also evident from the plot of the variation of the lift and moment coefficients as a function of the vortex position as shown in Fig. 10. This contrasts with incompressible behavior where the influence of the vortex is felt approximately equally far upstream and downstream of the airfoil.[27]

Comparison of pressure distributions for vortex-fixed and -moving cases shows that the unsteadiness greatly attenuates the influence of the vortex on the flow field around the airfoil, as shown in Fig. 11. The lift and drag coefficients for this example are $C_L = -0.06332$ and $C_D = 0.02186$ for the unsteady case and $C_L = -0.30152$ and $C_D = 0.04578$ for the quasi-steady case. The aerodynamic force coefficients for the quasi-steady case, thus, are significantly higher than the values for the unsteady case. The Mach number and pressure contours show the difference in quasi-steady and unsteady flow fields of such interaction. It is interesting to note that for the quasi-steady interaction of this vortex, vortex induced separation of the boundary layer was observed on the lower surface of the airfoil. But no separation was observed with the unsteady interaction of the same vortex.

### 3.3 Interaction of a Vortex with the NACA 64A006 Airfoil

The use of this airfoil has special significance because of the numerous numerical and experimental studies done with it. It is thinner than the NACA 0012 section and has significantly smaller leading-edge radius, so it will serve as a test case to check the applicability of the Transonic Small Disturbance equations particularly near the leading edge in the presence of vortex-induced downwash against Euler and Navier-Stokes equations which are exact.

Three cases are computed for this airfoil interacting with a moving Lamb-like vortex using the Euler and ATRAN2 codes, for the following conditions:

Case 1: $M_\infty = 0.85$, $\alpha = 0°$, $\Gamma = 0.2$,

$x_0 = -9.5$, $y_0 = -0.52$

Case 2: $M_\infty = 0.85$, $\alpha = 0°$, $\Gamma = 0.2$,

$x_0 = -9.5$, $y_0 = -0.26$

Case 3: $M_\infty = 0.85$, $\alpha = 0°$, $\Gamma = 0.4$,

$x_0 = -9.5$, $y_0 = -0.26$

Figures 12-17 summarize the results of these test cases. In all these cases, the airfoil incidence is zero and the dramatic difference in $C_p$ between the upper and lower surfaces is due solely to the vortex interaction. As before, the influence of the vortex is felt more on the lower surface of the airfoil than the upper surface, a result of nonlinear effects; linear small-distrubance calculations[4] showed the effects of the vortex to be equal and opposite on the upper and lower surface of the airfoil.

7

region; in the present case, upon the maximum value of $dy_b/dx$ at the grid point nearest the leading edge and on its variation at neighboring grid points. This unsatisfactory state of affairs is illustrated in Fig. 5a.

Keyfitz et al.[23] concluded that the errors in the small-disturbance results are due to the inherent approximations, and not to truncation errors. However, an improvement in the method can be obtained by introducing a simple correction in Eq. (17); namely, by replacing $Q_\infty$ by an analytical approximation to the local velocity $u$ near the leading edge. This is done in the spirit of a thin-airfoil blunt leading-edge correction, e.g., van Dyke,[24] who derived a uniformly valid second-order solution for the subsonic flow near parabolic leading edges. An excellent approximation to van Dyke's surface-speed distribution function $Q$ is

$$Q(x,r_\ell,M_\infty) \cong Q_\infty \sqrt{\frac{x}{x + r_\ell/2\beta}} \qquad (19)$$

where $\beta^2 = 1 - M_\infty^2$. Equation (19) reproduces van Dyke's theory exactly for incompressible flow. For compressible flow, Eq. (19) can be interpreted as effectively increasing the leading-edge bluntness in proportion to $1/\beta$. It may be mentioned in passing that this compressibility correction bears a superficial resemblance to the classical similarity rules of linearized thin-airfoil theory.[25] However, those rules are derived using the small-disturbance boundary condition, Eq. (17), and are therefore questionable with regard to the details of the flow in the leading-edge region.

Figure 5b shows the effect of replacing $\vec{Q}_\infty$ by Eq. (19) in the airfoil boundary condition, Eq. (17). This treatment renders the transonic small-disturbance solutions almost, but not completely, independent of the grid spacing. It also brings them into much better agreement with the Euler solutions. Accordingly, the results in this paper were obtained using this treatment.

## 3.  Results and Discussion

A two-dimensional approximation of helicopter blade-tip vortex encounter in forward flight with the following blade is obtained by simulating the interaction of a concentrated vortex with a stationary rotorcraft airfoil, as indicated in Fig. 2a. A vortex with a finite core and a Lamb-like analytical velocity distribution is considered to interact with the flow fields of NACA 0012 and NACA 64A006 airfoils. The cases of an interacting vortex fixed in space in the flow field (quasi-steady) as well as that convecting with the flow (unsteady) with the free stream velocity are considered. Viscous as well as inviscid flow field computations are performed. Thin layer Navier-Stokes equation set (Eq. (1)) is used for viscous flow field computations and Euler and ATRAN2 equation sets are used individually for inviscid flow field computations.

The numerical algorithm used for the viscous interacting flow field is given by Eq. (15). This is a perturbed form of the standard algorithm of Steger[2] where the disturbance or non-uniformity, $\hat{q}_o$, is supposed to be known. In the present study $\hat{q}_o$ is a solution of Euler equations that represents a vortex in a uniform flow. With the algorithm

Eq. (15), the boundary conditions are applied to the solution variable $\hat{q}$ instead of the perturbation quantity $(\hat{q} - \hat{q}_o)$. The advantage of this perturbation scheme is that it enables one to maintain accuracy even in a coarse far field grid. The non-uniformity does not have to be resolved in the coarse-grid outer flow. Near the body, however, the grid is fine enough to resolve both the non-uniform stream $(\hat{q}_o)$ and the deviation from it $(\hat{q} - \hat{q}_o)$. This approach was first suggested and successfully used by Buning and Steger[3] to calculate an inviscid shear flow past a cylinder.

### 3.1  Baseline Solutions

Baseline solutions represent the steady state solution of stationary airfoils in a uniform free stream. The airfoils considered are NACA 0012 in a free stream of Mach number 0.8 and at 0.5° angle of attack and NACA 64A006 at 0° angle of attack in a free stream of $M_\infty = 0.85$. For the thin layer Navier-Stokes solution, a nominal value of Reynolds number, based on the chord of the airfoil and free stream velocity, of 5.8 million is used. Turbulent boundary layer flow is assumed for the entire airfoil.

The baseline Navier-Stokes solution is computed by setting $\hat{q}_o \equiv 0$ in the algorithm, Eq. (15). In this case the numerical algorithm reduces to the standard (non-perturbed) form of Steger.[2] The baseline Euler solution is generated by turning-off viscous terms and setting $\hat{q} \equiv 0$ in Eq. (15) and in addition making suitable changes to accommodate surface boundary conditions. The baseline solution using Transonic Small Disturbance equations is obtained using ATRAN2 code,[4] which is a particular version of LTRAN2 code.[5] The steady state solution so obtained for the NACA 0012 airfoil is shown in Fig. 6 for the three methods in the form of plots of coefficient of pressure $(C_p)$. The agreement between the Navier-Stokes and Euler solutions is good, indicating that the viscous effects are relatively small for this case. However, ATRAN2 solution predicts the lower surface shock wave to be weaker and to occur upstream of that predicted by the Navier-Stokes and Euler codes. Nevertheless, all three methods give solutions which have good qualitative agreement.

### 3.2  Interaction of a Vortex with NACA 0012 Airfoil

(a) Vortex Fixed in Space. An analytical vortex, whose center is located at a point $(x_o, y_o)$ in the flow field as shown in Fig. 7a, is made to interact with the airfoil flow field. For Lamb-like vortex with a finite core and fixed in space, the cylindrical velocity distribution is given in the small disturbance limit for a compressible flow by

$$\frac{v_\theta(r)}{a_\infty} \cong \frac{\hat{\Gamma}}{r} \frac{\beta}{\cos^2 \theta + \beta^2 \sin \theta} (1 - e^{-r^2/a_o^2}) \qquad (20)$$

The velocity field from Eq. (20) and pressure field from Eq. (11) of the vortex are introduced into the airfoil flow field through the vector $\hat{q}_o$ in Eq. (15) and the resulting flow field is computed. Figure 8 shows steady state pressure distributions in the form of $C_p$ plots for this interaction computed from three methods for a vortex located at $x_o = 0.5$, $y_o = -1$ and of strength $\Gamma = 0.065$ ($C_{LV} = 0.13$). Comparison of pressure distributions of Fig. 8 with the baseline solutions,

6

Lindemuth and Killeen,[14] Briley and McDonald,[15,16] and Beam and Warming.[17,18] The procedure is a generalization of conservative, approximate factorization scheme in the "delta" form. The procedure has been successfully applied, for example, by Steger and Kutler,[19] Kutler et al.,[20] and Srinivasan et al.[21] for inviscid flows and by Steger[2] and Pulliam and Steger[22] for viscous flows. Use of the implicit procedure helps remove the stiffness of the problem introduced by a fine mesh.

As applied to Eq. (1) the implicit, spatially factored algorithm using Euler implicit time differencing takes the form

$$(I + h\delta_\xi \hat{A}^n - \epsilon_I J^{-1} \nabla_\xi \Delta_\xi J)$$

$$\times \; (I + h\delta_\eta \hat{B}^n + h\delta_\eta \hat{M}^n - \epsilon_I J^{-1} \nabla_\eta \Delta_\eta)(\Delta\hat{q}^n - \Delta\hat{q}_o^n)$$

$$= -\Delta t \left[ \delta_\xi(\hat{E}^n - E_o^n) + \delta_\eta(\hat{F}^n - \hat{F}_o^n) - Re^{-1} \delta_\eta \hat{S}^n \right]$$

$$- \epsilon_E J^{-1} \left[ (\nabla_\xi \Delta_\xi)^2 + (\nabla_\eta \Delta_\eta)^2 \right] J (\hat{q}^n - \hat{q}_o^n) \qquad (15)$$

where $\hat{A}$, $\hat{B}$, and $\hat{M}$ are the Jacobian matrices $\hat{A} = \partial E/\partial\hat{q}$, $\hat{B} = \partial\hat{F}/\partial\hat{q}$, $\hat{M} = \partial\hat{S}/\partial\hat{q}$ and I is the identity matrix. $\delta_\xi$, $\delta_\eta$ are the spatial central difference operators, $\Delta$ and $\nabla$ are forward and backward difference operators, e.g., $\Delta_\xi\hat{q} = \hat{q}(\xi + \Delta\xi,\eta) - \hat{q}(\xi,\eta)$ and for convenience $\Delta\xi = 1 = \Delta\eta$ is assumed. Indices denoting spatial location have been suppressed. The time index is denoted by n, t = (n $\Delta$t) corresponds to Euler implicit time differencing and $\hat{q}^n = \hat{q}(n\,\Delta t)$, $\hat{q}^n = (\hat{q}^{n+1} - \hat{q}^n)$. $\epsilon_I$ and $\epsilon_E$ are the implicit and explicit smoothing coefficients. In writing Eq. (15) it is assumed that $A_o \cong A$ and $B_o \cong B$ where $A_o = \partial E_o/\partial q_o$ and $B_o = \partial F_o/\partial q_o$.

Fourth-order dissipation terms such as $\epsilon_E J^{-1}(\nabla_\xi\Delta_\xi)^2 J(\hat{q} - \hat{q}_o)$ in Eq. (15) are added explicitly and these help to control possible numerical instabilities. The addition of the implicit second order difference terms, with coefficient $\epsilon_I$, operating on $(\Delta\hat{q}^n - \Delta\hat{q}_o^n)$ extends the linear stability bound of the fourth-order terms.[22]

Central differencing is used throughout the solution domain, except in regions of supersonic flow before a shock wave where upwind differencing is used. The use of upwinding for shocks is widespread in transonic potential calculations. Upwind differencing before shocks has a stabilizing effect and improves the accuracy of the calculations.

## 2.5 Transonic Small Disturbance Formulation

The unsteady transonic small-disturbance equation is based on the assumption of irrotational flow, which allows the velocity field $\vec{Q}$ to be expressed in terms of a potential. The vortex is introduced as a prescribed perturbation that is itself a solution to the Euler equation. Then the equation for the disturbance potential due to the airfoil itself becomes[4]

$$A\phi_{tt} + B\phi_{xt} = C_1\phi_{xx} + C_2(\phi_x + u_v)_x + \phi_{yy} \qquad (16)$$

where

$$A = M_\infty^2$$

$$B = 2M_\infty^2$$

$$C1 = 1 - M_\infty^2$$

$$C2 = -\frac{1}{2}(\gamma + 1)M_\infty^2$$

$$\vec{Q} = \vec{Q}_\infty + \nabla\phi + \vec{Q}_v$$

It is important to note that Eq. (16) is nonlinear and independent solutions are not superposable, but that the velocity field can still be split into three parts: 1) the (uniform) free stream, 2) a prescribed vortical disturbance, $\vec{Q}_v$, etc., and 3) the unknown disturbance potential $\nabla\phi$.

The usual small disturbance boundary conditions are flow tangency on the body, no disturbances at $x \to \infty$ and $y \to \pm\infty$, and $C_p = 0$ at $x \to \infty$. The new small-disturbance boundary condition on the body $y_b = F(x,t)$ (where $y_b = F(x,t)$ defines the airfoil surface), becomes

$$\left(\frac{\partial\phi}{\partial y}\right)_{y=0} = \vec{Q}_\infty \frac{dy_b}{dx} - \vec{J}v_v \qquad (17)$$

The wake behind the airfoil is represented by a branch cut through which vorticity convects from the airfoil to the downstream boundary. Across this branch cut the pressure is continuous; this is expressed as follows:

$$(\Gamma_x + \Gamma_t)_{wake} = 0 \qquad (18)$$

Equation (16) and its corresponding small-disturbance boundary conditions are solved by the Ames code ATRAN2,[4] which uses the basic time-accurate, implicit numerical algorithm of LTRAN2.[5] Further details of this code are described in Ref. 4.

## 2.6 Small-Disturbance Calculations in the Leading-Edge Region

The small-disturbance approximation has a well-known deficiency in the leading-edge region of airfoils, where neither the disturbance velocity $\Delta\phi$ nor the usual airfoil boundary condition, Eq. (17) is small enough to satisfy the basic premise of the theory.[23] The resultant loss of accuracy is often tolerable in other applications, but in the present vortex-interaction cases it poses a dilemma in interpreting the results for airfoils with small leading-edge radii. For example, the NACA 64A006 airfoil, with the leading edge radius $r_\ell/C \sim 0.0025$, exhibits a rapid expansion and suction peak very near the leading edge for small angles of attack or other vertical velocity perturbations. Accordingly, the small-disturbance results presented in Refs. 1 and 4 showed strong vortex-induced leading-edge peaks to form and collapse rapidly on the lower surface of this airfoil. If real, this phenomenon would seem to be a candidate source of acoustic radiation, such as the intense impulsive noise in helicopter aeroacoustics known as "blade-slap." Therefore, special attention was given to this point in comparing the small-disturbance and Euler results.

Two important facts quickly emerged in the comparison of numerical results. First, the Euler solutions showed much smaller magnitudes of the leading-edge pressure fluctuations, as will be seen. Secondly, as reported elsewhere,[23] the small-disturbance results were found to depend upon the computational grid spacing in the leading-edge

5

(usually free-stream value) and used to get e from Eq. (7). To ensure continuity across the wake cut a-b and d-e, the flow variables are linearly extrapolated from both sides of the cut and then averaged to obtain the values along the cut.

Along the body surface $\eta(x,y,t) = 0$, the no-slip condition for viscous flow without suction or injection is given by setting $V \equiv 0$ and $U \equiv 0$. The velocity components u and v are then calculated from

$$\begin{pmatrix} u \\ v \end{pmatrix} = J^{-1} \begin{bmatrix} \eta_y & -\xi_y \\ -\eta_x & \xi_x \end{bmatrix} \begin{pmatrix} -\xi_t \\ -\eta_t \end{pmatrix} \tag{8}$$

The pressure along the body surface is obtained from a normal momentum relation given by

$$P_n(\eta_x^2 + \eta_y^2)^{1/2} = J\rho(\partial_\tau \eta_t + u \, \partial_\tau \eta_x + v \, \partial_\tau \eta_y) \tag{9}$$

where $\eta$ is the direction normal to the body surface. This equation is solved implicitly in $\xi$ for pressure at the body. The density at the airfoil surface is obtained by extrapolation from the grid interior. Now since the pressure and density are known at the surface, the total energy is calculated from Eq. (7). The boundary conditions are of low order and hence require that the grid lines be clustered and normal at the body surface.

For the vortex interaction, a Lamb-like analytical vortex[8,9] with a finite core is specified. The cylindrical velocity of such a vortex is given for a compressible flow by

$$\frac{v_\theta(r)}{a_\infty} = \frac{\hat{\Gamma}}{r} (1 - e^{-r^2/a_o^2}) \tag{10}$$

where $v_\theta$ is the cylindrical velocity and is a function of only the radial distance r from the vortex center, $\hat{\Gamma} = \Gamma/2\pi a_\infty C$ is the dimensionless vortex strength, $a_o$ is the core radius, assumed equal to 0.05 in this study. For this vortex in a uniform free stream, the pressure field induced (by this vortex) is determined using the radial momentum equation

$$\frac{dp_v}{dr} = \frac{\rho_v v_\theta^2}{r} \tag{11}$$

in conjunction with the energy equation for constant enthalpy flow given by

$$\frac{\gamma}{\gamma - 1} \frac{P_v}{\rho_v} + \frac{1}{2} Q^2 = H_t \tag{12}$$

where $Q^2 = u^2 + v^2$ and $H_t$ is the total enthalpy. Once the pressure is known, density can be determined from Eq. (12). Having known the pressure and density, the total energy $e_v$ for the vortex is given by

$$e_v = \frac{P_v}{\gamma - 1} + \frac{1}{2} \rho_v Q^2 \tag{13}$$

This completes the determination of the vortex flow vector

$$\hat{q}_o = J^{-1} \begin{bmatrix} \rho \\ \rho u \\ \rho v \\ e \end{bmatrix}_v \tag{14}$$

## 2.3 Grid Generation

Surface conforming grids, that is, grids in which one coordinate falls on the body surface, are needed to simplify the application of the body boundary condition procedure and improve the overall accuracy of the numerical scheme. The grid generation process can be divided into several tasks: a) development of accurate surface representation, b) distribution of body surface points to yield a properly clustered, smoothly varying grid, and c) generation of outer boundary and interior mesh. While several methods of grid generation techniques are currently available (elliptic solver[10] and hyperbolic solver[11]), one that is suitable for the present application, based on past experience, is an algebraic method developed at Ames Research Center. The method has been discussed in detail by Pulliam et al.[12] and is based on the original algebraic grid generation technique of Eiseman[13]; the reader is referred to Pulliam et al.[12] for details. Briefly, the airfoil coordinates are taken as input and are used to define the airfoil surface. On the surface, grid points are distributed with clustering at the nose, trailing edge, and at prescribed locations along the upper and lower surfaces of the airfoil to resolve shocks. Coarse grid solutions can be used initially to determine the locations of shock waves. The grid lines are also clustered in the normal direction at the surface to resolve the boundary layer. This grid generation scheme is quite fast and will generate a 161 × 52 grid, say, around a NACA 0012 airfoil in less than 10 sec of CPU time on a VAX 11/780.

Several typical C-grids generated by this method are shown in Fig. 4 for NACA 0012 and NACA 64A006 airfoils. The grids of Figs. 4a and 4b are 161 × 52 in size and are for viscous flow computations of NACA 0012 airfoil and extend 6 chord lengths in all directions. The spacing of first node normal to the surface is $4 \times 10^{-5}$. The grid of Fig. 4c is for inviscid flow (Euler) computations of NACA 64A006 airfoil and has dimensions 181 × 45. The grid extends 10 chord lengths upstream and in y-direction and 6 chord lengths downstream of airfoil. The grid is clustered along the body surface and in the radial direction as shown in the figure. The spacing of the first node normal to the surface is $2 \times 10^{-3}$ chord. The grid of Fig. 4d is used for ATRAN2 computations of NACA 0012 airfoil. This is a 113 × 97 straight line grid extending 200 chord lengths in all directions with clustering at the leading and trailing edges as shown. The ATRAN2 grid used for the NACA 64A006 airfoil has the same spacing in the y-direction, but 186 points in the x-direction and finer clustering near the leading edge.

## 2.4 Numerical Algorithm

The numerical algorithm used to solve the conservation-law form of the thin-layer Navier-Stokes equations is based on a class of completely implicit noniterative, ADI schemes developed by

## 2. Numerical Formulations

### 2.1 Governing Equations

The governing partial differential equations are the unsteady, two-dimensional, thin layer Navier-Stokes equations.[2] These are written in non-dimensional, strong conservation-law form for a perfect gas using the generalized independent coordinate system of $\xi$, $\eta$, $\tau$ and in the perturbation form[3] as

$$\partial_\tau(\hat{q} - \hat{q}_o) + \partial_\xi(\hat{E} - \hat{E}_o) + \partial_\eta(\hat{F} - \hat{F}_o) = Re^{-1}\partial_\eta\hat{S} \qquad (1)$$

where

$$\hat{q} = J^{-1}\begin{bmatrix} \rho \\ \rho u \\ \rho v \\ e \end{bmatrix}$$

is the flow field vector we are solving for, $\hat{q}_o$ is the solution of the Euler equations $\partial_\tau\hat{q}_o + \partial_\xi\hat{E}_o + \partial_\eta\hat{F}_o = 0$ and, in this particular case, represents the solution of a prescribed vortex (either fixed in space or moving) in a uniform free stream. Also, the flux vectors $\hat{E}$, $\hat{F}$, and $\hat{S}$ are given by

$$\hat{E} = J^{-1}\begin{bmatrix} \rho U \\ \rho u U + \xi_x p \\ \rho v U + \xi_y p \\ (e + p)U - \xi_t p \end{bmatrix}, \quad \hat{F} = J^{-1}\begin{bmatrix} \rho V \\ \rho u V + \eta_x p \\ \rho v V + \eta_y p \\ (e + p)V - \eta_t p \end{bmatrix}$$

$$(2)$$

$$\hat{S} = J^{-1}\begin{bmatrix} 0 \\ \mu(\eta_x^2 + \eta_y^2)u_\eta + (\mu/3)\eta_x(\eta_x u_\eta + \eta_y v_\eta) \\ \mu(\eta_x^2 + \eta_y^2)v_\eta + (\mu/3)\eta_y(\eta_x u_\eta + \eta_y v_\eta) \\ \kappa Pr^{-1}(\gamma - 1)^{-1}(\eta_x^2 + \eta_y^2)\partial_\eta a^2 \\ + \mu(\eta_x^2 + \eta_y^2)(u^2 + v^2)_\eta/2 \\ + (\mu/3)(\eta_x u + \eta_y v)(\eta_x u_\eta + \eta_y v_\eta) \end{bmatrix}$$

$$(3)$$

where $U$ and $V$ are the contravariant velocities along the $\xi$ and $\eta$ directions given by

$$U = \xi_t + \xi_x u + \xi_y v$$

$$V = \eta_t + \eta_x u + \eta_y v$$

The matrices $\xi_t$, $\xi_x$, etc., are easily formed from the derivatives of $x_\tau$, $w_\xi$, etc., using the relations

$$\left.\begin{array}{ll} \xi_x = Jy_\eta & \eta_x = -Jy_\xi \\ \xi_y = -Jx_\eta & \eta_y = Jx_\xi \\ \xi_t = -x_\tau\xi_x - y_\tau\xi_y & \eta_t = -x_\tau\eta_x - y_\tau\eta_y \end{array}\right\} \qquad (4)$$

and $J$ is the transformation Jacobian given by

$$J = \xi_x\eta_y - \xi_y\eta_x = 1/(x_\xi y_\eta - x_\eta y_\xi) \qquad (5)$$

The metrics of Eq. (4) are not known analytically and therefore are to be determined numerically. To accomplish this, second-order central difference formulae are used at interior points and three-point one-sided formulae are used at the boundaries.

The viscous flux vector $S$ is written in the context of thin layer model[2] and hence is valid for high-Reynolds number turbulent flows. In the viscous stress terms of the flux vector $\hat{S}$, the viscosity coefficient $\mu$ is computed as the sum of $\mu_{laminar} + \mu_{turbulent}$ for turbulent boundary layer. Sutherland's equation[6] is used to evaluate $\mu_{laminar}$; the turbulent eddy viscosity, $\mu_{turbulent}$, is computed using a two-layer algebraic eddy viscosity model.[7]

The generalized coordinate system

$$\left.\begin{array}{l} \xi = \xi(x,y,t) \\ \eta = \eta(x,y,t) \\ \tau = \tau \end{array}\right\} \qquad (6)$$

allows the boundary surfaces in the physical plane to be mapped onto rectangular surfaces in the transformed plane as shown in Fig. 3. Moreover, this simplifies the procedure of grid point clustering in regions that experience rapid change in the flow field gradients. This is particularly important in the present problem because of the presence of the interacting vortex and shock waves.

The primitive variables of Eq. (1) are the density $\rho$, the mass fluxes $\rho u$, $\rho v$ in the two coordinate directions $x$ and $y$ and the total energy per unit volume $e$. In Eq. (2) $p$ represents the pressure, nondimensionalized by $\gamma p_\infty$; density $\rho$ by $\rho_\infty$; velocity components $u$, $v$ in $x$ and $y$ directions by $a_\infty$; and the energy $e$ by $\rho_\infty a_\infty^2$. The chord of the airfoil, $C$, is chosen as the reference length scale and is assumed equal to unity. The nondimensionalization also produces parameters such as Reynolds number (Re) and Prandtl number (Pr). The second coefficient of viscosity $\lambda$ is assumed equal to $-2/3\ \mu$, after Stokes hypothesis.

The pressure, density, and velocity components are related to the energy per unit volume by the equation of state which is written for a perfect gas as

$$e = \frac{p}{\gamma - 1} + \rho\left(\frac{u^2 + v^2}{2}\right) \qquad (7)$$

### 2.2 Boundary and Initial Conditions

Although Eq. (1) is solved for the perturbation quantity $(\hat{q} - \hat{q}_o)$, the boundary conditions are still applied only to the solution variable $\hat{q}$. $\hat{q}_o$, which is the solution of Euler equations, is supposed to be known, as described below.

The boundary conditions used are applied explicitly. Figure 3 shows a schematic of the solution domain. Along the outer boundary f-g-h freestream values are specified. At the outflow boundaries e-f and a-h, a simple linear extrapolation is used for $\rho$, $\rho u$, and $\rho v$. For supersonic flow the total energy $e$ is also extrapolated; but for subsonic flow pressure is held fixed to a constant

3

| $\kappa$ | = coefficient of thermal conductivity |
| --- | --- |
| $\lambda$ | = second coefficient of viscosity |
| $\mu$ | = coefficient of viscosity |
| $\xi,\eta,\tau$ | = transformed plane coordinates |
| $\xi_x,\xi_y,\ldots$ | = metrics of transformation |
| $\rho$ | = density |
| $\rho_\infty$ | = free stream density |
| $\phi$ | = disturbance potential |

Subscripts

| v | = refers to vortex |
| --- | --- |
| $\infty$ | = refers to free stream |

## 1. Introduction

The interaction of concentrated vortices with lifting surfaces is encountered in many aerodynamic and fluid dynamic applications. Although poorly understood, the interaction mechanism can have a significant influence on the aerodynamics, aeroelasticity, and aeroacoustics of maneuvering vehicles and especially so in the transonic flow regime. This is because in transonic flow the shock wave position and strength are sensitive to small changes in the flow parameters. Of particular interest, in the present study, is the interaction encountered in a helicopter rotor flow field. The interaction of a trailing vortex wake in such a flow field with the oncoming rotor blades can induce unsteady blade loading and aerodynamic noise. The blade tips, which trail strong and concentrated tip vortices, trace out prolate cycloidal paths in space, leading to a variety of possible blade-vortex interactions. The generic problem, shown schematically in Fig. 1, can be viewed as an unsteady, three-dimensional close encounter of a curved-line vortex, at an arbitrary intersection angle $\Lambda$, with a high aspect-ratio lifting surface that is executing combined rotational and translational motion at transonic speeds. The limiting cases of such encounter for $\Lambda = 0°$ and $90°$ are illustrated in Figs. 2a and 2b, respectively; the former encounter is essentially two-dimensional but unsteady, whereas the latter can be considered as steady but highly three-dimensional. For more discussion of these representations and their aeroacoustic implications, the reader is referred to a recent paper by George and Chang.[1]

Under certain flight conditions, helicopter rotor produces an impulsive, highly directional noise at a regular frequency corresponding to the blade passage frequency. At least two mechanisms are thought to be responsible for this impulsive noise, also called the "blade slap": 1) shock formation on the advancing side of the blade due to local transonic flow, and 2) unsteady lift fluctuations on the blade due to interaction of the tip vortex from the preceding blade. In order to shed some light on the understanding of this second mechanism (corresponding to the case of Fig. 2a), the present study prepared groundwork for a future aeroacoustic and vibratory airloads computation capability by making unsteady two-dimensional flow-

field computations of a vortex interaction with a stationary rotorcraft airfoil.

Current numerical algorithms to compute unsteady transonic vortical flows of the helicopter rotor are frequently either inadequate or too costly to use for routine design analysis of a large class of two- and three-dimensional flow fields. Unsteady potential theory cannot be satisfactorily used for such analyses unless major assumptions are made in modeling the nonlinear vortex wake structure. Numerical algorithms based on the Euler equations are suitable for any inviscid flow field simulation but cannot be applied to flows dominated by viscous effects, in which case the only choice is to use the Navier-Stokes equations. But current numerical algorithms for both Euler and Navier-Stokes equations used for unsteady flow computations have large computer time and storage requirements.

The motivation for the present study is twofold. The first of these is to apply a modified form of Euler and thin layer Navier-Stokes twodimensional codes for computing the rotational compressible flow field of the interaction of a vortex with a stationary rotorcraft airfoil made up of either NACA 0012 or NACA 64A006 profiles. The cases of interacting vortex fixed in space in the flow field as well as convecting past the airfoil will be considered so as to better understand the flow phenomenon and to provide benchmark solutions for checking out more approximate engineering prediction techniques. The second objective is to further the methodology of existing numerical procedures so that advanced simulations of full helicopter flow fields are possible when more powerful computers become available.

With the above objectives in mind, an implicit finite difference procedure for solving the unsteady, two-dimensional thin layer Navier-Stokes equations in conservation-law form of Steger[2] was modified to implement the perturbation scheme of Buning and Steger[3] to resolve non-uniform incoming streams (vortex in the present study) without having to specify far-field grid refinement. This was further modified to include the quasi-steady (vortex fixed) and unsteady (vortex free) vortex effects to compute the interaction flow field. Although the concentrated vortex is analytically specified and preserved in this study, an actual experimental vortex can easily be substituted in its place. (It should be mentioned that the code has the provision to turn off viscosity and modify the boundary conditions to make Euler calculations if and when needed.)

Parallel computations of this interacting flow field are also done using ATRAN2 code[4] (transonic small disturbance approximation to the velocity potential equation). ATRAN2 code is a modification of Ballhaus and Goorjian's LTRAN2 code[5] to include the high frequency term $\phi_{tt}$ and concentrated or distributed rotational disturbances in the flow field.

In this paper the numerical formulations are discussed in Section 2. Results and discussion are presented in Section 3 and the conclusions are summarized in Section 4.

# NUMERICAL SIMULATION OF THE INTERACTION OF A VORTEX WITH STATIONARY AIRFOIL IN TRANSONIC FLOW

G. R. Srinivasan*
Flow Simulations, Inc., Sunnyvale, California

W. J. McCroskey† and P. Kutler‡
NASA Ames Research Center, Moffett Field, California

### Abstract

A perturbation form of an implicit conservative, noniterative numerical algorithm for the two-dimensional thin layer Navier-Stokes and Euler equations is used to compute the interaction flow field of a vortex with stationary airfoil. A Lamb-like analytical vortex having a finite core is chosen to interact with a thick (NACA 0012) and a thin (NACA 64A006) airfoil independently in transonic flow. Two different configurations of vortex interaction are studied, viz., 1) when the vortex is fixed at one location in the flow field; and 2) when the vortex is convecting past the airfoil at free stream velocity. Parallel computations of this interacting flow field are also done using a version of the Transonic Small Disturbance Code (ATRAN2). A special treatment of the leading edge region for thin airfoils is included in this code. With this, the three methods gave qualitatively similar results for the weaker interactions considered in this study. However, the strongest interactions considered proved to be beyond the capabilities of the small disturbance code. The results also show a far greater influence of the vortex on the airfoil flow field when the vortex is stationary than when it is convecting with the flow.

### Nomenclature

$\hat{A}, \hat{B}$ = Jacobian matrices

$a_0$ = vortex core radius

$a_\infty$ = free stream sound speed

$C$ = characteristic length scale, chord of the airfoil

$C_D$ = drag coefficient

$C_L$ = lift coefficient

$C_{LV}$ = lift equivalent vortex strength

$C_P$ = coefficient of pressure

$\hat{E}, \hat{E}_0$ = flux vectors

$e$ = total energy per unit volume

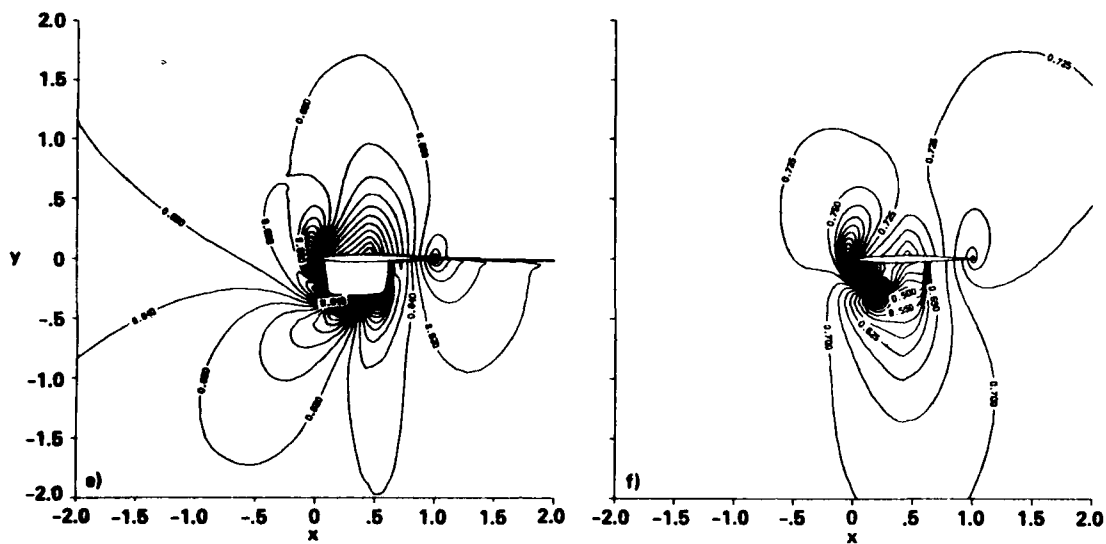$\hat{F}, \hat{F}_0$ = flux vectors

$H_t$ = total enthalpy

$I$ = identity matrix

$J$ = transformation Jacobian

$M_\infty$ = free stream Mach number

$Pr$ = Prandtl number

$p$ = pressure

$p_\infty$ = free stream static pressure

$\vec{Q}$ = velocity vector

$\vec{Q}_v$ = velocity induced by the vortex, $iu_v + jv_v$

$Q_\infty$ = free stream velocity

$\hat{q}$ = unknown flow field vector

$\hat{q}_0$ = Euler solution of vortex in a uniform free stream

$Re$ = Reynolds number

$r$ = radial distance from the vortex center

$\vec{r}_0$ = initial position of the vortex, $ix_0 + jy_0$

$r_\ell$ = airfoil leading edge radius

$\hat{S}$ = viscous flux vector

$U, V$ = contravariant velocity components

$u_\infty$ = free stream x-velocity

$u, v$ = velocity components in physical plane in x and y directions

$u_v, v_v$ = velocity components induced by the vortex in x and y directions

$v_\theta$ = circumferential direction

$x_0, y_0$ = initial vortex location in the flow field

$x_v, y_v$ = instantaneous position of the vortex

$x, y, t$ = physical plane coordinates

$\alpha$ = angle of attack

$\beta$ = compressibility factor, $(1 - M_\infty^2)^{1/2}$

$\gamma$ = ratio of specific heats

$\Gamma$ = strength of vortex

$\varepsilon_E, \varepsilon_I$ = smoothing coefficients

$\theta$ = the angle which the vortex velocity vector makes with y-axis

---

*Senior Research Engineer. Member AIAA.
†Senior Staff Scientist, U.S. Army Aeromechanics Laboratory and NASA Thermo- and Gas-Dynamics Division. Associate Fellow AIAA.
‡Chief, Applied Computational Aerodynamics Branch. Associate Fellow AIAA.

(e) Mach number contours.

(f) Pressure contours.

$\Gamma = 0.4$ ($C_{LV} = 0.8$), $x_v = 0.2$, $y_v = -0.26$.

Fig. 17 Concluded.

21

(e) Mach number contours.                    (f) Pressure contours.

$\Gamma = 0.4$ ($C_{LV} = 0.8$), $x_v = 0.2$, $y_v = -0.26$.

Fig. 17  Concluded.

# END

# FILMED

11-85

# DTIC